Infiltration of cell-inspired ultra-deformable magnetic microrobots in restrictive environments

Eugenia De Remigis, Fehmi M. Dikbaş, Michele Ibrahimi, Francesco Bianciardi, Elisa L. Petrocelli, Elisa Roberti, Veronica Iacovacci, *Member, IEEE*, Stefano Palagi, *Member, IEEE*.

Abstract—Microscale robotics represents a promising future for minimally invasive medicine. However, one of the biggest challenges of microrobots moving through the human body is represented by the complex 3D structure of biological lumina and tissues, which obstructs the navigation of micron-sized devices. Here, we fabricate ultra-deformable magnetic microrobots, consisting of ferrofluid-loaded lipid vesicles, and we magnetically pull them through chambers that exert upon them a gradually more forceful confinement. We thus analyze their capability to face interstices comparable to or smaller than their characteristic size and their consequent behavior in terms of stability, velocity, and deformation. The results show that the inherent compliance of these vesicle-based magnetic microrobots allows them to infiltrate successfully in interstices slightly smaller than their size. Further enhancement of their compliance and the development of specific control strategies may lead to microrobots able to move through interstices and traverse complex biological environments.

Index Terms—Bio-inspired robotics, magnetic devices, mobile robots, soft robotics, vesicles.

I. INTRODUCTION

THANKS to the advancements in technology, minimally invasive medicine is increasingly gaining ground in medical practice. In this ever-evolving field, microscale robotics can offer the revolutionary potential to build untethered devices that can reach remote areas of the human body otherwise inaccessible and perform diagnostic or therapeutic actions in an extremely localized way, significantly reducing the damages on tissues and the recovery time for patients [1].

However, to reach their target site, such devices need to navigate through cavities as small as a few microns, such as blood capillaries, and eventually extravasate and travel through biological tissues. Such spaces are filled not only with various concentrations of cells, but also with biological fluids and extracellular matrices, made of networks of macromolecules and other chemical compounds. This results in non-trivial

E. De Remigis (e-mail: eugenia.deremigis@santannapisa.it), M. Ibrahimi, F. Bianciardi, E. Roberti, V. Iacovacci, S. Palagi (phone: +39 050 883055; e-mail: stefano.palagi@santannapisa.it) are with the BioRobotics Institute, Sant'Anna School of Advanced Studies, Viale Rinaldo Piaggio 34, Pontedera (Pisa), 56025, Italy.

F. M. Dikbaş is with the Department of Electronics, Information and Bioengineering, Polytechnic University of Milan, Milan, 20133, Italy.

E. L. Petrocelli was with the Civil and Industrial Engineering Department, Sapienza University of Rome, Rome, 00185, Italy.

rheological properties, interstices that are often in the sub-micrometer scale [2]–[4], and possible interactions with the molecules constituting the network [5].

A proposed solution to the challenge of infiltrating and navigating such complex 3D environments is to reduce one or more device dimension to the nanoscale: magnetically-driven, helical propellers with sub-micron diameter, smaller than typical tissue pores, have been proved to move efficiently through different types of environments [6], possibly facilitated by smart coatings that minimize interactions with network structures [5]. The nanoscale, however, poses severe limitations to the complexity and capabilities that a device can be endowed with. This has partially been addressed by designing dynamical swarms of nanoparticles [7], capable of more degrees of freedom and higher loading capability than single nano-devices; actuating these swarms, however, requires complex and finely tuned control strategies.

Nanoparticle-based organic ferrofluid has been employed for the fabrication of magnetically controlled liquid droplets with remarkable capabilities of deformation (up to an aspect ratio of 9 [8]) and shape adaptability [9]–[12]. However, these droplets are in the millimeter scale and rely on splitting into sub-droplets to navigate smaller spaces, thus losing body integrity. Moreover, while the solid component of ferrofluid is biocompatible and biodegradable, the organic carrier fluid can compromise biocompatibility; hence an aqueous carrier would be preferable for microrobotics applications [13].

The outstanding abilities of living microstructures can suggest compromise solutions to these issues: leukocytes, for example, are fundamental agents of our immune system, capable of migrating in narrow vessels and through dense tissues. They have been the inspiration to design swarms of nanoparticles capable of rolling along channel walls [14]. In this work, we take inspiration from another remarkable characteristic of leukocytes: their ability to squeeze through interstices smaller than their characteristic size to extravasate and navigate through tissues. This is thanks to a migration strategy called amoeboid locomotion [2], [15], [16], based on a continuous adaptation to and exploitation of the surrounding environment through large body deformations. We thus design and fabricate ultra-deformable magnetic microrobots by loading cell membrane-inspired vesicles with an aqueous ferrofluid. This allows for significant deformation without loss of integrity. The vesicle membrane consists of a phospholipid bilayer just a few nanometers thick, imitating the structure and composition of the plasma membrane of natural cells. This, together with the liquid nature of the vesicle content, results

in extreme compliance and adaptability of the microrobots. We fabricate two types of micro-structured chambers with a gradually narrowing channel, comparable or smaller than the characteristic size of the microrobots. By employing a magnetic field, we guide the microrobots through, imposing a gradually more forceful confinement. We analyze the effects of confinement on stability, velocity, and deformation, to understand how the passive compliance given by the soft structure can be exploited to navigate through restrictive environments.

II. MATERIALS AND METHODS

A. Materials

1,2-dioleoyl-sn-glycero-3-phosphocholine (DOPC) in chloroform (CAS 4235-95-4), mineral oil (CAS 8042-47-5), D-(+)-glucose and sucrose were purchased from Merck. Custom-made aqueous ferrofluid (20% Iron Oxide nanoparticles) was purchased from Qfluidics. For aqueous solutions, MilliQ water is used unless differently stated (Elix® Advantage 10 Water Purification System). Permanent magnets (NdFeB, N42 grade, $8\,\text{mm} \times 15\,\text{mm} \times 15\,\text{mm}$) were purchased from Supermagnete. Formlabs Surgical Guide Resin was used for the production of chambers.

B. Characterization of ferrofluid

In order to build a descriptive model to quantify the effect of the applied magnetic field on the microrobots, magnetic properties of ferrofluid are determined through vibrating-sample magnetometry (VSM) (MicroSense EZ7 Vibrating Sample Magnetometer) within a field of $\pm 1.9\,\text{T}$. The obtained raw data are fitted with a 2-parameter sigmoidal function with the Julia programming language on Visual Studio Code (LsqFit package [17]):

$$M(B) = p_1 \cdot \arctan(p_2 x). \tag{1}$$

From this fitting equation, the magnetization at saturation M_s and the volume susceptibility χ_{lin} are obtained respectively as the value of $M(B)$ for $B \to +\infty$ and the value of the first derivative in $B = 0$.

C. Preparation of magnetic vesicles

Vesicles containing ferrofluid are prepared through the droplet transfer method [18], [19]: $100\,\mu\text{l}$ of a pre-warmed ($50\,°\text{C}$, $30\,\text{min}$) oil phase containing $2.5\,\text{mg/ml}$ DOPC dissolved in mineral oil is pipetted on top of $300\,\mu\text{l}$ of a $240\,\text{mM}$ glucose solution in a $1.5\,\text{ml}$ tube; then, a 2.5% water-in-oil emulsion is prepared in another tube by vortexing $5\,\mu\text{l}$ of an aqueous phase (2:1 $240\,\text{mM}$ sucrose solution : ferrofluid) in $200\,\mu\text{l}$ of the same oil phase and pipetted on top of the oil layer in the first tube; the sample is then centrifuged (Sigma 1-14K refrigerated microcentrifuge) at room temperature for $60\,\text{min}$ at $500\,\text{g}$. The passage of the emulsion droplets through the oil film containing phospholipids allows for the formation of a lipid bilayer encapsulating the aqueous phase. The remaining oil phase is removed by pipetting and the sample is transferred to a clean vial. To perform a size selection of the microrobots, enough time is allowed for the larger ones to spontaneously

sediment due to gravity, after which the aqueous medium is removed and substituted by fresh one. The suspension is then topped up to $1\,\text{ml}$ to have an appropriate microrobot concentration for the experiments. The samples can be stored at $4\,°\text{C}$ for up to a week.

The lipidic membrane separates the aqueous ferrofluid from the environment, preventing the dispersion of the ferrofluid and of the hydrophilic nanoparticles in the aqueous environment and ensuring microrobot integrity.

D. Infiltration experiments

We designed and performed infiltration experiments to understand whether the microrobots could move through narrow spaces and to which extent. Moreover, we aimed to observe the effect of different levels of restriction severity on the stability of the microrobots and their behavior in terms of deformation and velocity. For image acquisition, a Hirox digital microscope (Hirox HRX-01) is used. The experiments consist in the infiltration of the microrobots in restrictive chambers under the magnetic force exerted by a permanent magnet. The setup consists of two parts: a chamber and a support, which holds the chamber and the magnet. The support allows to fix the position of the magnet with respect to the sample and the position of both with respect to the reference frame of the microscope.

Preliminarily, non-restrictive experiments were performed to confirm the hypothesis that the applied field could induce deformation and movement of the microrobots, and to find the optimal distance between the magnet and the sample to observe such phenomena. For these experiments, the chamber consisted of an adhesive frame (Gene Frame, $25\,\mu\text{l}$, ThermoFischer Scientific) stuck on a microscopy slide, covered by a glass cover slip; this created a channel with a fixed height of $250\,\mu\text{m}$. We define this condition as "free space", as the height is at least 5 times the characteristic dimension of observed microrobots. These experiments were also used as control to validate the proposed model for the force and velocity calculations.

Next, we performed restrictive experiments. Considering the average dimensions of our microrobots, we designed two types of chambers that we define as "soft confinement" and "hard confinement" respectively. Both chambers were designed on Autodesk Fusion 360 and printed with a Formlabs 3D printer (Form 3B+) using Surgical Guide Resin, chosen for its translucence. The design of a chamber is illustrated in Fig. 1 and consists of a narrow channel of width $1.5\,\text{mm}$ and length $20\,\text{mm}$, confined by two supports for a microscopy cover slip. We define two ends for the channel: a proximal one (closer to the magnet) and a distal one (further from the magnet); at the proximal end of the channel, a stopper element is designed for the cover slip to lie against. The height of the supports gradually decreases along the length of the channel, towards the proximal end, creating a gradually more forceful confinement. For the soft confinement condition, the height degrades from $h_{max} = 500\,\mu\text{m}$ to $h_{min} = 25\,\mu\text{m}$, which is comparable to the typical diameter of a microrobot; for the hard confinement, it degrades from $h_{max} = 500\,\mu\text{m}$ to $h_{min} = 0\,\mu\text{m}$. To ensure

This article has been accepted for publication in IEEE Transactions on Medical Robotics and Bionics. This is the author's version which has not been fully edited and content may change prior to final publication. Citation information: DOI 10.1109/TMRB.2024.3503898
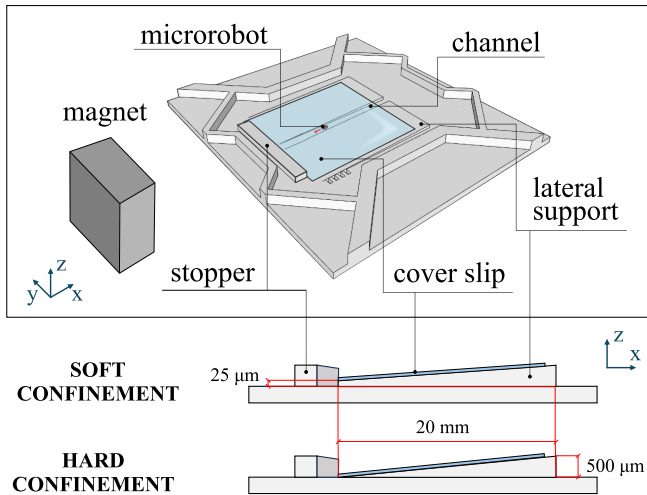
3

Fig. 1. Top: general design of a restriction chamber. Bottom: relevant sections of the soft and hard confinement chambers respectively; for ease of visualization, the sections are not at scale.
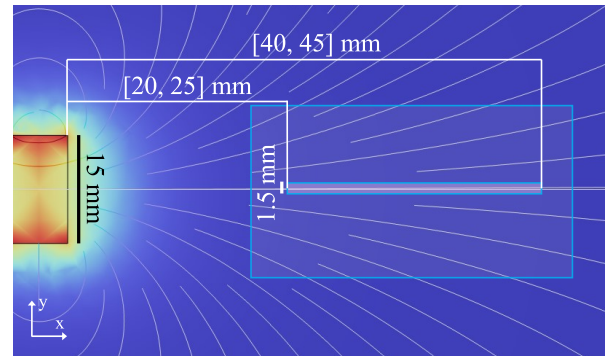

Fig. 2. Schematic of the experimental setup for infiltration experiments; the positions of the chamber and channel (right) are represented with respect to the magnet (left) and the resulting field streamlines.

that the height of the channel corresponded to the design value, the microscopy cover slip was glued on top of the supports using cyanoacrylate glue (Loctite® Super Attak). The design allows us to calculate the height of the channel at any point along the x-axis as $h(x) = (x - x_0) \cdot \tan(\alpha)$, where x_0 is the position of the stopper (i.e. the proximal end of the channel) and α is the tilt angle of the chambers, calculated as $\alpha = \arctan((h_{max} - h_{min})/L)$, with L the total length of the supports. Hence, we are able to relate the observed behavior of microrobots at any position to the corresponding confinement level.

After the chamber is mounted on the support, the positions of the magnet (x_M) and of the proximal end of the channel (x_0) are registered in the microscope reference system. Then, $2.5\,\mu l$ of $240\,mM$ glucose solution is pipetted in the channel, then $5\,\mu l$ of microrobots suspension is added, and finally more glucose solution is added to ensure the chamber is completely filled and thus avoid the formation of a meniscus in the channel. When the sample is stable (no convection observed), the magnet is inserted into the support and the movement of the microrobots is imaged; multiple videos are taken for each microrobot at a framerate of 12 fps, following its path until its stopping point.

E. Field simulation

The magnetic field generated by the permanent magnet is modeled with the Finite Element Method (COMSOL Multiphysics® 6.1) to calculate the field and gradient values at any observable point. The work plane is defined as the xy-plane with the origin at the center of the magnet. The simulation performs a 3D Stationary study of the *Magnetic Fields, No Currents* physics module. The 3D magnetic flux density $B = (B_x, B_y, B_z)$ generated by the magnet is calculated at a distance range covering the whole experimental setup, with a step width of $0.1\,mm$. The setup allows to position the chamber so that the channel is aligned with the axis of the magnet (Fig. 2); considering the width and maximum height

of the channel ($1.5\,mm$ and $0.5\,mm$ respectively), it can be assumed that any point on the observed space lies roughly on the axis of the magnet (parallel to the x-axis), therefore the y- and z-components are considered negligible.

F. Modeling of the microrobot movement

The model of the velocity of the microrobot is built in Julia on Visual Studio Code. The theoretical velocity of the microrobots is calculated through the Stokes equation for low Reynolds number conditions:

$$v_{theor}(x) = \frac{1}{6\pi\mu r} \cdot F_m(x), \tag{2}$$

where μ is the fluid dynamic viscosity, ($\sim 1\,mPa\,s$ for a $240\,mM$ glucose solution at a temperature of $25\,°C$ [20], [21]), r is the radius of the section of the microrobot perpendicular to the movement.

To calculate the magnetic force F_m applied to the microrobot, we consider the magnetic moment m_m, which depends on the volume of the microrobot V and the volume susceptibility χ. In general, χ is a function of the field and consequently of the position, but we assume it to be in the linear part of the hysteresis curve and hence constant. The magnetic moment is thus expressed as:

$$m_m(x) = V\chi B(x), \tag{3}$$

As regards the volume, considering the composition of the microrobots core (2:1 sucrose : ferrofluid), the theoretical effective volume of the ferrofluid is 1/3 of the total volume of the microrobot, hence in (3) we have that $V \equiv V_{eff,theor} = V_{geom}/3$.

Given these considerations, the force exerted on the microrobot by the magnetic field and gradient can be expressed as:

$$F_m(x) = 2V\chi B(x) \cdot \nabla B(x), \tag{4}$$

where $\nabla B(x)$ is the gradient of the magnetic flux density.

To obtain the field gradient, the magnetic flux density $B(x)$ is interpolated through a cubic spline of the simulated data (Dierckx package [22], [23]); then the gradient is calculated as the first derivative of the field along the x-axis: $\nabla B \equiv dB/dx$.

Lastly, to calculate the predicted velocity of the microrobot, we consider two possible approximations for the radius r in

This article has been accepted for publication in IEEE Transactions on Medical Robotics and Bionics. This is the author's version which has not been fully edited and content may change prior to final publication. Citation information: DOI 10.1109/TMRB.2024.3503898

4

(2). At first, we use a spherical approximation, where we assume that the elongation along the x-axis corresponds to a shortening that is equal on the y- and z-axes, such that $r_z \equiv r_y$; hence, we calculate r as the equivalent radius of a sphere with the same volume as the microrobot (spherical approximation) $r \equiv r_{eq} = \sqrt[3]{r_x r_y^2}$. Then, we consider an ellipsoidal correction: due to the elongation, the radius of the section perpendicular to the movement can become significantly smaller than the equivalent radius; to account for this, we consider $r \equiv r_y$.

G. Data analysis

The data analysis is performed through Julia on Visual Studio Code. The goal of the data analysis is to quantify the empirical velocity of the microrobots and their deformation at each point, and to relate them to the intensity of the corresponding magnetic field and the entity of confinement.

The tracking of each microrobot is performed through a frame-by-frame ellipse detection algorithm (OpenCV package [24]); this gives the coordinates of the centroid of the ellipse traced around the microrobot (x_μ, y_μ), the sizes of the semi-axes $(r_x(x), r_y(x))$ and the tilt angle of the ellipse with respect to the x-axis $\theta(x)$. All ellipses are considered aligned with their major axis along the x-axis $(\theta(x) \equiv 0)$.

In order to quantify the confinement that the microrobot is subjected to at a given location, we define a parameter, the relative height of the confinement $c(x) = h(x)/d$, which relates the height of the channel at a given point $h(x)$ to the characteristic size of the microrobot, its diameter $d = 2r$. To generalize this value with respect to the possible deformation of the magnetic microrobot, the radius is calculated as per the spherical approximation.

To quantify the deformation of the microrobot along its path, we calculate its aspect ratio $a_r(x) = r_x(x)/r_y(x)$; considering the geometry of the problem, $a_r \in [1, +\infty)$.

Finally, the position of the microrobot with respect to the magnet is calculated as $x = x_\mu - x_M$. The empirical velocity v_{emp} is calculated numerically at each point as:

$$v_{emp,i} = \frac{x_i - x_{i-1}}{t_i - t_{i-1}}, \tag{5}$$

and smoothing is performed to remove the calculation noise (Smoothing package [25], [26]).

To compare the empirical velocity with the theoretical one, another phenomenon must be considered: the droplet transfer method does not guarantee a homogenous distribution of the ferrofluid; hence, a different and microrobot-specific concentration of ferrofluid is expected. To account for this dilution, a correction factor γ is calculated for each microrobot through linear regression between the theoretical and empirical velocities; the effective volume of ferrofluid is then adjusted through this correction factor: $V_{eff} = V_{eff,theor}/\gamma$ and the theoretical velocity is recalculated considering $V \equiv V_{eff}$ in (4). The model error is calculated on free-space experiments as the root mean square error (RMSE) between predicted and measured values.
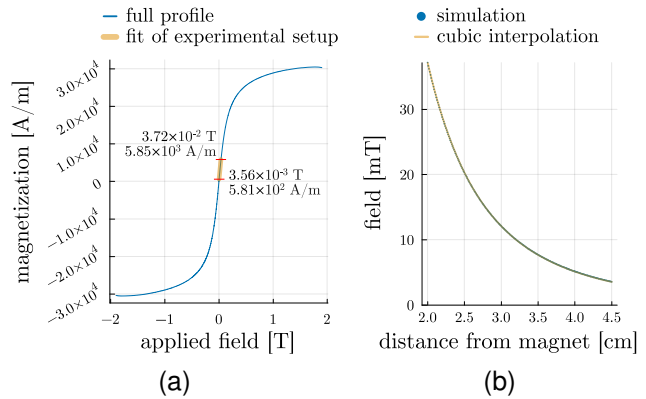

Fig. 3. (a) Hysteresis curve of ferrofluid; the region highlighted in yellow represents the portion of interest, corresponding to the field applied in the experimental setup. (b) Simulation of the field applied in the experimental setup and its corresponding cubic interpolation.

III. RESULTS AND DISCUSSION

A. Magnetic characterization

The magnetization curve obtained from the VSM analysis is pictured in Fig. 3a. The profile of the curve confirms that the ferrofluid displays superparamagnetic behavior. The saturation magnetization is $M_S = 3.18 \times 10^4$ A/m and the volume susceptibility in the linear section is $\chi_{lin} = 1.39 \times 10^5$ A/(m T). The experimental field is calculated for the optimal distance from the magnet between 20 and 45 mm; the curve obtained through COMSOL simulation and the corresponding interpolation are shown in Fig. 3b. The field applied in the experimental setup never allows to reach saturation magnetization but it is entirely included in the linear section of the magnetization profile (Fig. 3a), hence in (3) we can confirm that for our experiments $\chi \equiv \chi_{lin}$.

B. Model validation

In order to validate the model described in paragraph II-F, the theoretical and empirical velocities are compared for the free-space condition. Both models make an accurate prediction (relative RMSE $< 6.5\%$); for a moderate deformation (median $a_r = 1.65$), the spherical approximation displays a slightly lower RMSE than the ellipsoid approximation, with an RMSE of ± 2.84 µm/s and ± 3.99 µm/s respectively; this may be due to the fact that the spherical model is less prone to errors caused by fluctuations in the detection of the axes of the microrobot. An example of free-space velocity comparison is displayed in Fig. 4.

C. Infiltration capability

The microrobots obtained through the droplet-transfer method ranged in size between 5 and 35 µm and displayed various concentrations of ferrofluid (Fig. 5); size selection removed microrobots under ~ 15 µm. The mean diameter of microrobots used for infiltration experiments was 23 ± 5 µm.

Free-space experiments confirmed that the applied field induces both deformation and movement of microrobots. The maximum velocity achieved by the microrobots depended not
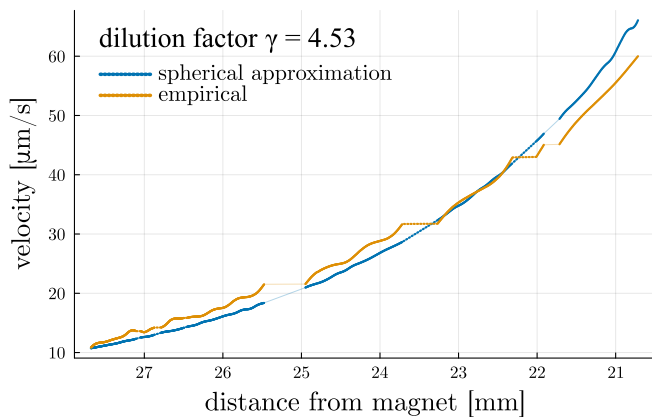
Fig. 4. Comparison between the predicted velocity profile of the microrobot (after dilution correction) and the measured velocity.
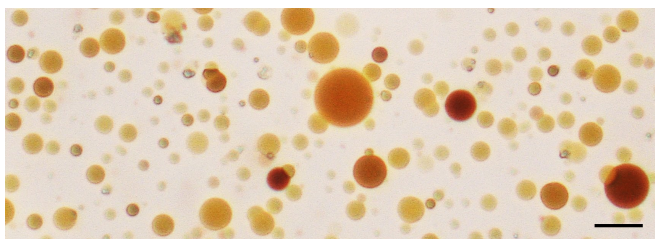

Fig. 5. Optical microscopy image of the microrobots, representative of the sample before size selection and dilution. The nanometer-thick lipidic membrane separates aqueous ferrofluid from the environment, ensuring integrity. Darker color indicates higher ferrofluid concentration. Scalebar is $20\,\mu m$.

only on the size, but also on the dilution factor: e.g. under a field of $33.8\,mT$ a microrobot with $r_{eq} = 8.7\,\mu m$ and $\gamma = 4.5$ reached a maximum velocity of $60\,\mu m/s$, while one with $r_{eq} = 10.2\,\mu m$ and $\gamma = 2.2$ reached a maximum velocity of $101.1\,\mu m/s$.

In the described experimental conditions, microrobots have been observed to infiltrate interstices as small as 1/4 of their characteristic size. Two distinct behaviors have been observed in conditions of soft and hard confinement.

1) Microrobot stability: Breakage of microrobots along the channel has been observed in only $\sim 6\%$ of the analyzed cases, for any entity of deformation, and never in free space condition. In order to test resistance to the constriction of confinement, when microrobots reach their stopping point, the magnet was moved closer to the chamber to increase the magnetic force; applying a stronger field did not result in a further infiltration, but showed that microrobots are able to withstand a force of at least $2.78\,nN$ in conditions of strict confinement without breakage.

2) Soft confinement: In the case of soft confinement, the most restrictive condition the microrobots undergo is comparable to their characteristic size ($h(x_0) \approx d$); the minimum relative height of confinement $c(x_0)$ ranged between 0.91 and 1.37.

The microrobots were successfully able to infiltrate the channel throughout its entire length, only stopping in correspondence of the stopper element. For $c(x) \geq 1.5$, the empirical velocity roughly follows the profile of the predicted
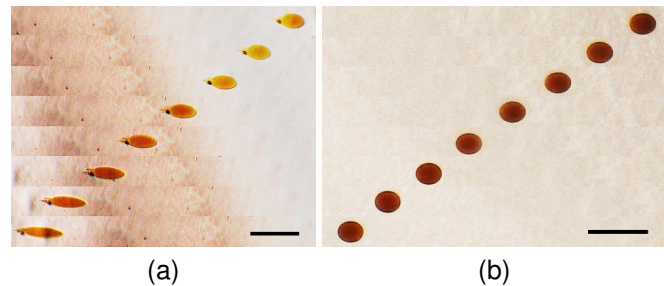

Fig. 6. Sequences of frames depicting the deformation of microrobots in soft confinement (a) and hard confinement (b) while they move along the channel. Scalebars are $50\,\mu m$ and $100\,\mu m$ respectively. Frames have been shifted on the horizontal axis for ease of visualization.

velocity, then the profiles diverge.

Here, extreme deformations, up to an aspect ratio of over 4.5 (Fig. 6a and 7), can be observed even in a condition of semi-confinement, i.e. before microrobots are constricted directly by the channel walls ($1 < c(x) < 1.5$); in turn, these extreme deformations lead to a significant reduction of the diameter of the microrobot section perpendicular to the movement direction ($r \equiv r_y$ in (2)), with a consequent increase in velocity above the predicted free-space value (Fig. 8a). When microrobots eventually undergo a confinement comparable or smaller than their diameter, a drop in velocity can be observed, while the deformation reaches its maximum.

The observed deformation is comparable to values reported for millimeter scale organic ferrofluid droplets [10]–[12], but [27] reports experimental values up to $a_r \approx 20$ for microscale droplets. To understand whether this deformation is due solely to the magnetic field, we compared this behavior to that of microrobots subjected to the same field intensity but in free space; in this case, only a moderate deformation is observed, which, after a rapid increase, reaches a maximum value of 2.17 and then remains circa constant at any field intensity (Fig. 7). This suggests that confinement, however soft, plays a crucial role in the deformation.

3) Hard confinement: In the case of hard confinement, at the proximal section of the channel the microrobots face an interstice of dimension significantly smaller than their diameter ($h(x \rightarrow x_0) \ll d$).

In this case, the microrobots were able to move into the interstice but stopped before reaching x_0 ($h(x_0) = 0$); the maximum infiltration capability observed corresponded to a minimum relative height of $c(x) = 0.26$. Here, the empirical velocity again follows the predicted profile for $c(x) \geq 1.5$, but the measured velocity starts decreasing in the semi-confinement region ($1 < c(x) < 1.5$), while a steeper drop is observed under direct confinement ($c(x) \leq 1$), until the microrobot stops moving (Fig. 8b). Remarkably, before stopping definitively, microrobots display small oscillations in their x-positions, as if trying to infiltrate further. In terms of deformation, when the field is applied, the aspect ratio of the microrobots rapidly increases, but quickly reaches a maximum value of 2.10, comparable to that of free space (see III-C2). Remarkably, with the increase of confinement, the deformation gradually decreases to a minimum of 1.81, and
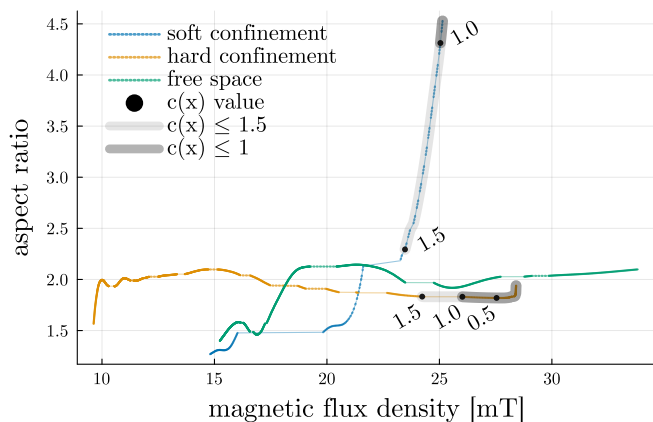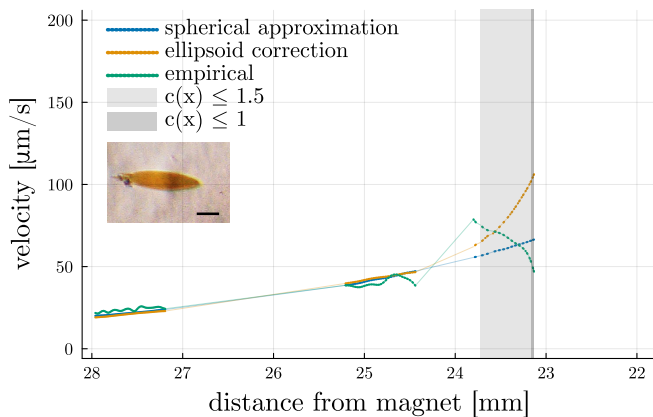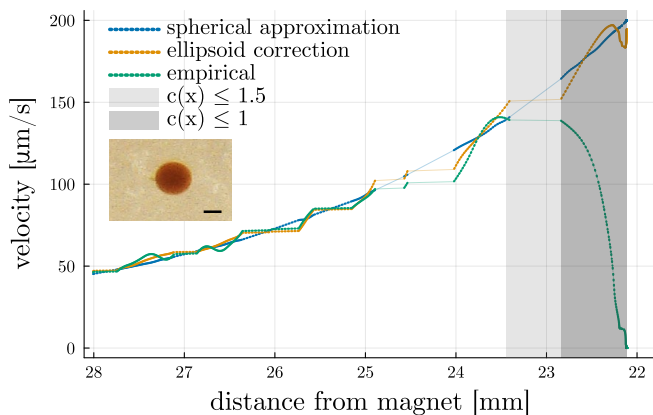
Fig. 7. Profiles of measured aspect ratio for microrobots in soft and hard confinement and in free space, as a function of the applied field; the comparison highlights that the magnetic flux density is not the sole responsible for the deformation.

(a)

(b)

Fig. 8. Comparisons of predicted velocity (spherical and ellipsoidal approximations) and empirical velocity in soft (a) and hard confinement (b) conditions. The appended microscopy images display the deformation of microrobots at the stopping point. Scalebars are $20\,\mu m$.

no extreme deformations are observed (Fig. 6b and 7). When the microrobot stops, the aspect ratio again slightly increases to 1.94, which could be interpreted as a further stretch in an attempt to infiltrate the confined space under the pull of the magnetic force.

IV. CONCLUSION

In this work, we tested and analyzed the capability of ultra-deformable magnetic microrobots to infiltrate restrictive environments. We demonstrated that the vesicle-based microrobots are able to significantly and reversibly deform to move through interstices with one dimension up to four times smaller than their diameter without breakage.

While strict confinement consistently caused a rapid and significant decrease in velocity, we observed two different behaviors in terms of deformation, which in turn influenced velocity in regions of milder confinement. We observed that significant deformation, not explainable solely by the magnetic field strength, occurs in case of soft confinement before the microrobot is directly constricted by the channel walls; we speculate this to be due to a type of wall effect influencing the interaction of the microrobot with the thin fluid layer interposed between its body and the channel walls. Further investigating this phenomenon and its influence on deformation and velocity can help develop more complex models to eventually induce controllable deformations. The design of more complex test environments, such as obstacle courses and irregular 3D cavities, will help assess the capability of the microrobots to navigate 3D environments.

DOPC-based membranes are highly biocompatible and stable in saline buffers [28], [29]; this, together with the biocompatibility of the aqueous ferrofluid [13] makes these microrobots promising candidates for medical applications. Further study of the stability within more complex fluids and cell cultures will help elucidate the possibility of interactions with biological fluids and tissues, and the possible need for optimization of the chemical composition of the microrobots.

Further enhancement of the compliance of lipid vesicle-based microrobots and the development of specific magnetic actuation and control strategies able to exploit it may lead to a new generation of magnetic microrobots capable of moving through network interstices and traverse complex biological environments.

REFERENCES

[1] D. Liu, T. Wang, and Y. Lu, "Untethered Microrobots for Active Drug Delivery: From Rational Design to Clinical Settings," *Advanced Healthcare Materials*, vol. 11, no. 3, p. 2102253, 2022, _eprint: https://onlinelibrary.wiley.com/doi/pdf/10.1002/adhm.202102253. [Online]. Available: https://onlinelibrary.wiley.com/doi/abs/10.1002/adhm.202102253

[2] P. Friedl and B. Weigelin, "Interstitial leukocyte migration and immune function," *Nat Immunol*, vol. 9, no. 9, pp. 960–969, Sep. 2008.

[3] K. Wolf, M. te Lindert, M. Krause, S. Alexander, J. te Riet, A. L. Willis, R. M. Hoffman, C. G. Figdor, S. J. Weiss, and P. Friedl, "Physical limits of cell migration: Control by ECM space and nuclear deformation and tuning by proteolysis and traction force," *Journal of Cell Biology*, vol. 201, no. 7, pp. 1069–1084, Jun. 2013. [Online]. Available: https://doi.org/10.1083/jcb.201210152

[4] T. Lämmermann and R. N. Germain, "The multiple faces of leukocyte interstitial migration," *Semin Immunopathol*, vol. 36, no. 2, pp. 227–251, Mar. 2014. [Online]. Available: https://www.ncbi.nlm.nih.gov/pmc/articles/PMC4118216/

[5] Z. Wu, J. Troll, H.-H. Jeong, Q. Wei, M. Stang, F. Ziemssen, Z. Wang, M. Dong, S. Schnichels, T. Qiu, and P. Fischer, "A swarm of slippery micropropellers penetrates the vitreous body of the eye," *Science Advances*, vol. 4, no. 11, p. eaat4388, Nov. 2018, publisher: American Association for the Advancement of Science. [Online]. Available: https://www.science.org/doi/10.1126/sciadv.aat4388

[6] D. Schamel, A. G. Mark, J. G. Gibbs, C. Miksch, K. I. Morozov, A. M. Leshansky, and P. Fischer, "Nanopropellers and Their Actuation in Complex Viscoelastic Media," *ACS Nano*, vol. 8, no. 9, pp. 8794–8801, Sep. 2014, publisher: American Chemical Society. [Online]. Available: https://doi.org/10.1021/nn502360t

[7] J. Yu, L. Yang, X. Du, H. Chen, T. Xu, and L. Zhang, "Adaptive Pattern and Motion Control of Magnetic Microrobotic Swarms," *IEEE Transactions on Robotics*, vol. 38, no. 3, pp. 1552–1570, Jun. 2022, conference Name: IEEE Transactions on Robotics. [Online]. Available: https://ieeexplore.ieee.org/abstract/document/9653146

[8] M. Sun, B. Hao, S. Yang, X. Wang, C. Majidi, and L. Zhang, "Exploiting ferrofluidic wetting for miniature soft machines," *Nat Commun*, vol. 13, no. 1, p. 7919, Dec. 2022, publisher: Nature Publishing Group. [Online]. Available: https://www.nature.com/articles/s41467-022-35646-y

[9] M. Sun, S. Yang, J. Jiang, and L. Zhang, "Horizontal and Vertical Coalescent Microrobotic Collectives Using Ferrofluid Droplets," *Advanced Materials*, vol. 35, no. 23, p. 2300521, 2023, _eprint: https://onlinelibrary.wiley.com/doi/pdf/10.1002/adma.202300521. [Online]. Available: https://onlinelibrary.wiley.com/doi/abs/10.1002/adma.202300521

[10] R. Ahmed, M. Ilami, J. Bant, B. Beigzadeh, and H. Marvi, "A Shapeshifting Ferrofluidic Robot," *Soft Robotics*, vol. 8, no. 6, pp. 687–698, Dec. 2021, publisher: Mary Ann Liebert, Inc., publishers. [Online]. Available: https://www.liebertpub.com/doi/full/10.1089/soro.2019.0184

[11] X. Fan, X. Dong, A. C. Karacakol, H. Xie, and M. Sitti, "Reconfigurable multifunctional ferrofluid droplet robots," *Proceedings of the National Academy of Sciences*, vol. 117, no. 45, pp. 27916–27926, Nov. 2020, publisher: Proceedings of the National Academy of Sciences. [Online]. Available: https://www.pnas.org/doi/full/10.1073/pnas.2016388117

[12] S. Afkhami, A. J. Tyler, Y. Renardy, M. Renardy, T. G. S. Pierre, R. C. Woodward, and J. S. Riffle, "Deformation of a hydrophobic ferrofluid droplet suspended in a viscous medium under uniform magnetic fields," *Journal of Fluid Mechanics*, vol. 663, pp. 358–384, Nov. 2010. [Online]. Available: https://doi.org/10.1017/S0022112010003551

[13] A. Joseph and S. Mathew, "Ferrofluids: Synthetic Strategies, Stabilization, Physicochemical Features, Characterization, and Applications," *ChemPlusChem*, vol. 79, no. 10, pp. 1382–1420, 2014, _eprint: https://onlinelibrary.wiley.com/doi/pdf/10.1002/cplu.201402202. [Online]. Available: https://onlinelibrary.wiley.com/doi/abs/10.1002/cplu.201402202

[14] M. Mihlan, K. M. Glaser, M. W. Epple, and T. Lämmermann, "Neutrophils: Amoeboid Migration and Swarming Dynamics in Tissues," *Frontiers in Cell and Developmental Biology*, vol. 10, Apr. 2022, publisher: Frontiers Media SA. [Online]. Available: /pmc/articles/PMC9038224/

[15] A. Callan-Jones, "Self-organization in amoeboid motility," *Frontiers in cell and developmental biology*, vol. 10, Oct. 2022, publisher: Front Cell Dev Biol. [Online]. Available: https://pubmed.ncbi.nlm.nih.gov/36313569/

[16] T. Lämmermann, B. L. Bader, S. J. Monkley, T. Worbs, R. Wedlich-Söldner, K. Hirsch, M. Keller, R. Förster, D. R. Critchley, R. Fässler, and M. Sixt, "Rapid leukocyte migration by integrin-independent flowing and squeezing," *Nature*, vol. 453, no. 7191, pp. 51–55, May 2008, publisher: Nature Publishing Group.

[17] P. K. Mogensen, "JuliaNLSolvers/LsqFit.jl," Feb. 2024, original-date: 2014-05-31T20:57:57Z. [Online]. Available: https://github.com/JuliaNLSolvers/LsqFit.jl

[18] S. Pautot, B. J. Frisken, and D. A. Weitz, "Production of Unilamellar Vesicles Using an Inverted Emulsion," *Langmuir*, vol. 19, no. 7, pp. 2870–2879, Apr. 2003. [Online]. Available: https://pubs.acs.org/doi/10.1021/la026100v

[19] A. Moga, N. Yandrapalli, R. Dimova, and T. Robinson, "Optimization of the Inverted Emulsion Method for High-Yield Production of Biomimetic Giant Unilamellar Vesicles," *ChemBioChem*, vol. 20, no. 20, pp. 2674–2682, Oct. 2019. [Online]. Available: https://chemistry-europe.onlinelibrary.wiley.com/doi/10.1002/cbic.201900529

[20] K. Zhuo, Q. Liu, Y. Wang, Q. Ren, and J. Wang, "Volumetric and Viscosity Properties of Monosaccharides in Aqueous Amino Acid Solutions at 298.15 K," *J. Chem. Eng. Data*, vol. 51, no. 3, pp. 919–927, May 2006, publisher: American Chemical Society. [Online]. Available: https://doi.org/10.1021/je050412t

[21] "Chemical and physical properties of Glucose + Water." [Online]. Available: https://www.chemeo.com/mid/11-074-h/Glucose_Water

[22] K. Barbary, "kbarbary/Dierckx.jl," Feb. 2024, original-date: 2014-10-15T06:28:03Z. [Online]. Available: https://github.com/kbarbary/Dierckx.jl

[23] "Curve and Surface Fitting with Splines." [Online]. Available: https://www.netlib.org/dierckx/

[24] "JuliaImages/OpenCV.jl," Nov. 2023, original-date: 2021-06-17T17:32:10Z. [Online]. Available: https://github.com/JuliaImages/OpenCV.jl

[25] P. Nakroshis, "paulnakroshis/Smoothing.jl," Nov. 2022, original-date: 2021-11-17T20:31:57Z. [Online]. Available: https://github.com/paulnakroshis/Smoothing.jl

[26] P. Marchand and L. Marmet, "Binomial smoothing filter: A way to avoid some pitfalls of least-squares polynomial smoothing," *Review of Scientific Instruments*, vol. 54, no. 8, pp. 1034–1041, Aug. 1983. [Online]. Available: https://doi.org/10.1063/1.1137498

[27] J.-C. Bacri and D. Salin, "Instability of ferrofluid magnetic drops under magnetic field," *J. Phys. Lett.*, vol. 43, Sep. 1982.

[28] D.-H. Won, S.-Y. Kim, G.-N. Lim, and S.-N. Park, "A Study on the Stability of DOPC Liposome," *Journal of the Society of Cosmetic Scientists of Korea*, vol. 37, no. 1, pp. 55–60, 2011, publisher: Society of Cosmetic Scientists of Korea. [Online]. Available: https://koreascience.kr/article/JAKO201117463446352.page

[29] F. Wang and J. Liu, "Nanodiamond decorated liposomes as highly biocompatible delivery vehicles and a comparison with carbon nanotubes and graphene oxide," *Nanoscale*, vol. 5, no. 24, pp. 12375–12382, Nov. 2013, publisher: The Royal Society of Chemistry. [Online]. Available: https://pubs.rsc.org/en/content/articlelanding/2013/nr/c3nr04143c